3

COMPUTATIONAL INDUSTRIAL MECHANICS PROGRAMME

Sophisticated mathematical modelling aided by powerful computing and visualization has the potential to provide the cutting-edge to industry; generation of cost-effective solutions, process optimization and product design are some of the areas where modelling and simulation can play critical to enabling role. The C-MMACS Computational Industrial Mechanics Programme (CIMP) seeks to develop and apply tools of mathematical modelling and computer simulation in diverse areas of engineering.

Inside

3.1 Evidence of Some Determinism in Microtremor Data

Waves emitted by seismic sources such as explosions or earthquakes have been used to measure the travel time of body waves, the dispersion curves of surface waves and the frequencies of the Earth's normal modes. Inversion of those measurements provide some fundamental information about the Earth's interior and allows us to understand the Earth's structure both in terms of its spherically symmetric stratification and in terms of the three-dimensional and anisotropic variations of seismic properties (Shapiro and Campillo, 2004). Major research efforts are being dedicated to two related questions. The first question is whether nonlinear dynamics can be used to gain a better understanding and interpretation of observed complex dynamical behavior. The second is whether nonlinear dynamics can yield advantages in predicting or controlling such time evolution. The time evolution of a system property can be measured by recording a time series. Nonlinear time series techniques when applied to such time series may provide partial answers to the above questions.

The microtremor data used in this study were collected from two different sources which were located at a distance of around 30m apart. These data were collected at a sampling rate of 100 HZ using a Lennartz LE-3D (5 sec) seismometer and a City-Shark-II data acquisition system. In this study, we have analyzed 35 time series data, 10 from the first source and 25 from the second. Every file has three component time series, vertical, north-south and east-west. All the files are separated into three individual files before analyzing them one by one.

We applied several methods to verify the presence of some determinism in the time series data. These methods include the autocorrelation of a time series, the recurrence plot, the power spectrum, the nonlinear prediction of the successive values and the Hurst exponent. Some programs used in this study are taken from the TISEAN software package (Hegger et al., 1999).

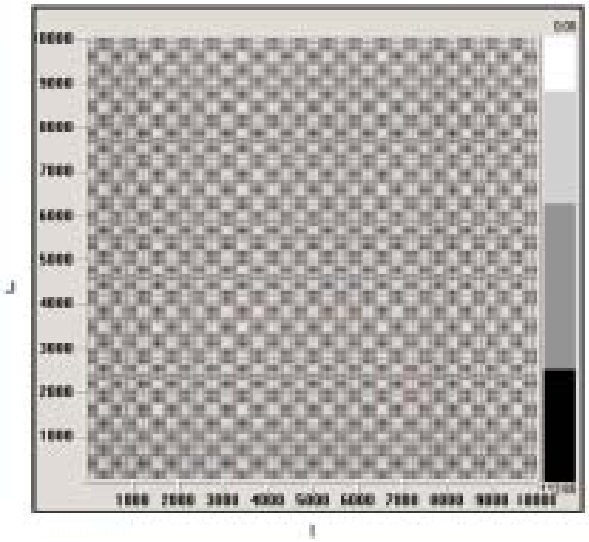

Figure 3.1. Recurrence plot of the Vertical component of a typical Microtremor data. A regular pattern in the figure indicates a deterministic component in the data.

Recurrence analysis

Recurrence plots are a useful tool to identify structure in a data set in a time resolved way qualitatively. This can be intermittency (which one detects also by direct inspection), the temporary vicinity of a chaotic trajectory to an unstable periodic orbit, or non-stationarity. Recurrence Plots (RPs) were first described in 1987 (Eckmann et al., 1987). With a RP, one can detect hidden patterns and structural changes in data or see similarities in patterns across the time series under study. A recurrence plot of the vertical component of a typical time series data is plotted in figure 3.1 using VRA (Kononov, 2006). The recurrence plot of this data is plotted using an embedding dimension of 3 and time delay of 1, which are in some sense the most appropriate values for the data sets we have analyzed. A repetitive formation of grey color squares in this plot indicates that after a certain period some pattern is found in the time series. This

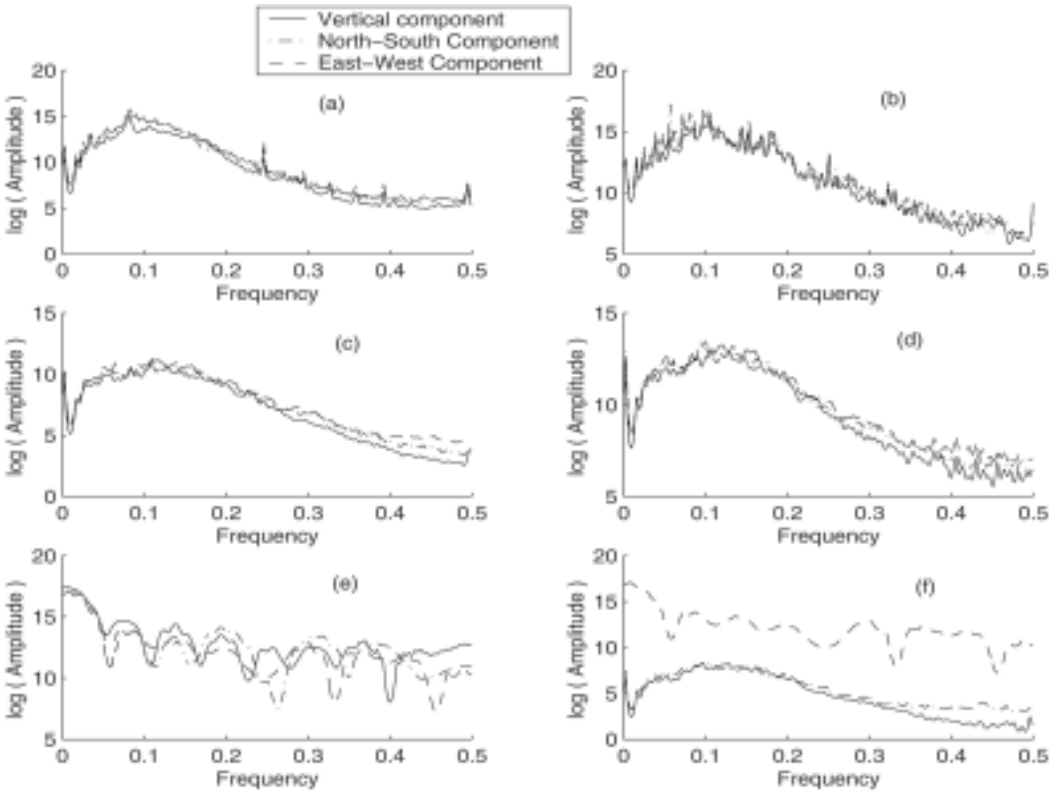

Figure 3.2. Power spectrum of all three components of six microtremor data. An exponentially decaying powerspectrum indicates either a linear noise process or a chaotic process. Periodic data will yield spikes in the figures.

indicates the presence of some structure in this data.

Time delay

The time delay was determined in three different ways. First is the space time separation plot (Provenzale et al., 1992). Using a space time separation plot the value of the product of the time delay and the embedding dimension came out to be approximately eight. The second method is an autocorrelation plot. The minimum value of the delay (in an autocorrelation plot) where the autocorrelation of a given time series first goes to zero is a value of the time delay for that time series. Using the autocorrelation plot we obtained a time delay of approximately 8. The third method to estimate a time delay is by using time series forecasting. In this method we predict values of a time series in future. The combination which yields the minimum prediction error gives an estimate of the value of the time delay and the embedding dimension. The time delay calculated from the prediction error of the time series came out to be unity. However, it was noticed that a change of time delay only leads to a very small change in the output. Hence for all future tests we use a time delay of unity.

Embedding Dimension

The embedding dimension is calculated using the minimum prediction error of the time series. We used different embedding dimensions to calculate the prediction error. The minimum error was achieved for all the time series at an embedding dimension of 3 and time delay of 1. Therefore, the embedding dimension was taken to be 3. Here, we used an embedding dimension of 3 and time delay of 1 for the analysis of all the time series.

Power Spectrum

The Power Spectrum plot gives an estimate of the signal strength of the data at different

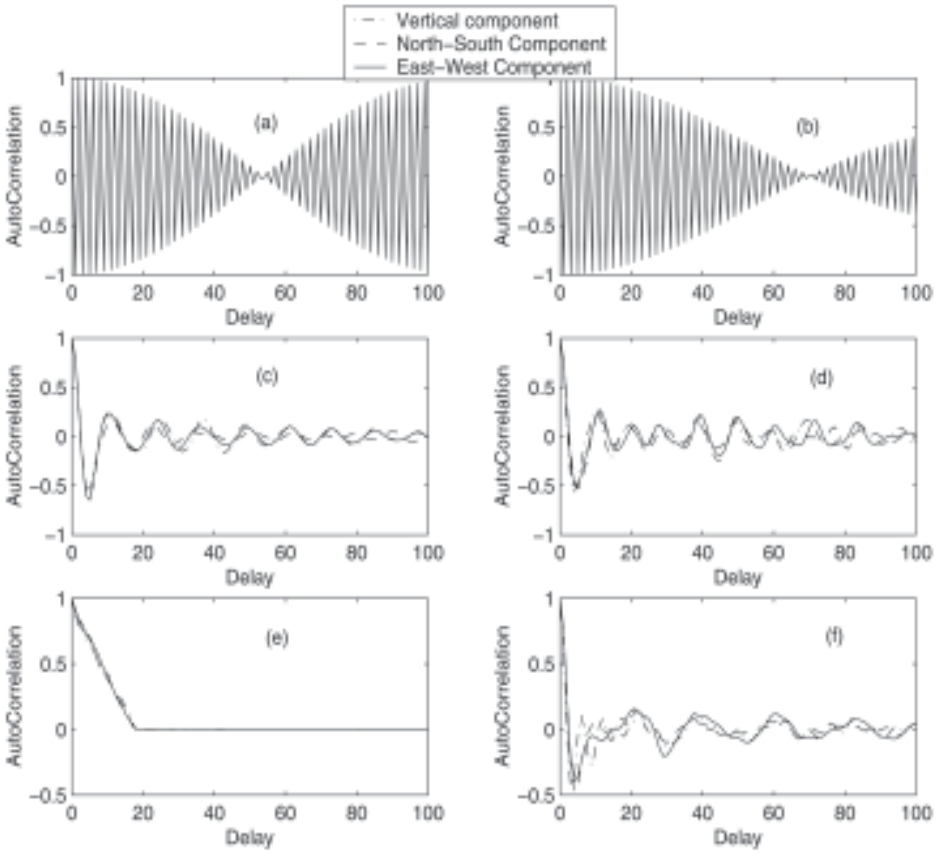

Figure 3.3 Power spectrum of all three components of six microtremor data. An exponentially decaying powerspectrum indicates either a linear noise process or a chaotic process. Periodic data will yield spikes in the figures.

frequencies. The strength of the signal at high frequencies is usually considered as being due to noise. In Figure 3.2 we have plotted the power spectrum of all the three component data (vertical, north-south and east-west) for six time series taking a log scale on the vertical axis (amplitude). Since high frequency data is considered as a form of noise that means the relative strength of the signal at high frequency will decide how noisy the data is. In figures 3.2 (a), (b), (c) and (d) the power spectrum of different microtremor data is plotted.

The power is increasing with increase in frequency until a frequency of 0.1 after that it decreases. At high frequencies the amplitude saturates at a minimum value. This indicates that data has an appreciable deterministic component as the amplitude is different at different frequencies. Figure 3.2 (e) and (f) give the power spectrum of two different microtremor data. The amplitude remains almost the same for all frequencies. This indicates that there is only weak determinism in these two data sets. We note that the power spectrum of almost all the time series is similar to those shown in figures 3.2 (a), (b), (c) and (d).

Autocorrelation

The autocorrelation for all the three axis data was calculated and plotted in figure 3.3 for six different microtremor data. Figure 3.3 (a) and (b) indicate strong determinism since autocorrelation is high for all delay and there is little saturation. We note that the autocorrelation goes to zero after a delay of 55 and 70 for figure 3.3 (a) and (b) respectively. Figure 3.3 (c) and (d) are the autocorrelation plots of two different microtremor data. The autocorrelation fluctuates and then saturates at zero after delay 100. This indicates appreciable

determinism in the time series. We note here that almost all the time series exhibit behaviour similar to that shown in Figure 3.3 (c) and (d). We also note that autocorrelation goes to zero after a delay of 3 or 4. This yields a time delay value of 3 for both these microtremor data. Figure 3.3 (e) and 3(f) show the autocorrelation plot of two other microtremor time series. In figure 3.3 (e) the autocorrelation saturates after delay 20. This indicates weak determinism in the time series. Similarly figure 3.3 (f) also indicates weak determinism in this microtremor data.

Test for Chaos

In this method, the one-step ahead forecasting error is computed as a function of the number of nearest neighbors (k) used to form the forecast.

In figure 3.4 the number of neighbors vs. the prediction error of the vertical component of a typical time series (10,000 data points) is plotted. One step ahead prediction is performed using a number of neighbors ranging from 20 to 200 in steps of 10. Such an error plot is repeated for all combinations of time delay 1 to 3 and embedding dimension 3 to 5. Since the prediction error increases with increase in number of neighbors it shows some indications of chaos (For chaotic data the prediction error should increase exponentially with increase in number of neighbors).

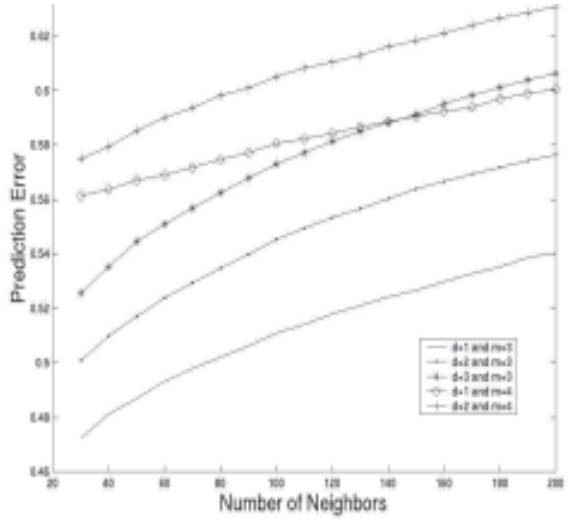

Figure 3.4 Prediction error vs. number of neighbors plot of vertical component of a typical microtremor data.

In this work we have applied some of the tools of nonlinear time series analysis to microtremor data to demonstrate the presence of a deterministic component in almost all the microtremor data we have analyzed. Microtremor data sets were collected from two sites in Ahmedabad, India. First linear tools were used to visualize the data. These visual tools indicated the presence of a pattern in the time series. This suggests that the time series is not completely white noise. Nonlinear tools including nonlinear prediction were used to verify that the data has some structure.

Vikas Krishnia, T R Ramamohan and Imtiyaz A Parvez

3.2 The effect of Inertia on the Dynamics of a Periodically Forced Spherical Particle in a Quiescent Fluid

We study the effect of inertia on the dynamics of a periodically forced spherical particle in a quiescent fluid. In this problem, we have initially considered the spherical particle to be neutrally buoyant. The only source for its motion is the external periodic force applied onto the spherical particle. We study the effects of both convective inertia and unsteady inertia using the expression for hydrodynamic force given by Lovalenti and Brady (1993). We note that in the expression given by Lovalenti and Brady (1993), the inclusion of inertia results in additional terms in the equation governing the dynamics of the particle that represent a fading memory for the entire history of the motion. The inclusion of convective inertia in the low Reynolds number limit makes the memory term nonlinear.

In 2006-2007, we formulated the problem using the expression of Lovalenti and Brady (1993). The equations governing the motion of a periodically forced spherical particle in a quiescent fluid are:

$$\frac{dY_p}{dt} = U_p$$

$$\frac{dU_p}{dt} = \frac{1}{\mathrm{Re}^*}\left[\mathrm{Re}_F \sin t - 6\pi (U_p - U_0) + \frac{3}{8}\left(\frac{\mathrm{Re}\, Sl}{\pi}\right)^{1/2}(J_1 + I_1)\right]$$

Where,

$$J_1 = 16\pi (U_p(t) - U_0)\left[\frac{1}{\sqrt{t}} - \frac{1}{\sqrt{\varepsilon}}\right]$$

$$I_1 = \int_0^{t-\varepsilon}\left\{\frac{1}{A^2}\left(\frac{\sqrt{\pi}}{2|A|}erf(A) - \exp(-A^2)\right)\right\}\frac{12\pi (U_p(s) - U_0)}{(t-s)^{3/2}}ds$$

Here, *Re* represents the Reynolds Number, Y_p is the particle displacement, U_p is the Velocity of the particle $A = \frac{\mathrm{Re}}{2}\left(\frac{t-s}{\mathrm{Re}\, Sl}\right)^{1/2}\left(\frac{Y_S(t) - Y_S(s)}{t-s}\right)$, *Sl* is the Strouhal Number, Re_F is the amplitude of the periodic forcing term.

We generated a few results. One of our main results was that the particle had a drift velocity and thus formed a solenoidal attractor. In 2007 we sent this result for publication to Physics of Fluids. They questioned our result, observing that it might be a numerical artifact. However, we could not prove the validity of our result as they were not explained by the physics of the problem.

Current work

We evaluated the software carefully and rectified it to obtain results to satisfy the physics. We obtained a number of interesting results. These results satisfied the earlier tests which we had performed on the software and also were physically explainable. Our earlier

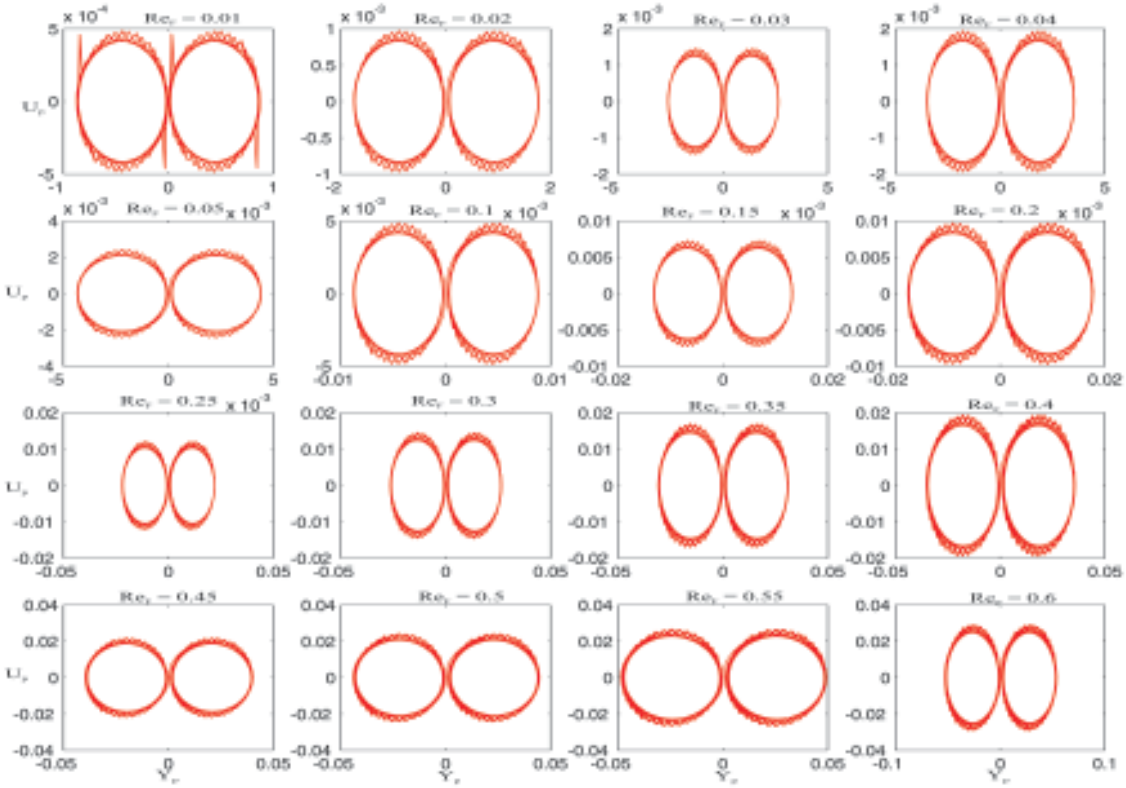

Figure 3.5 Plots of the dimensionless velocity versus dimensionless position for different values of ReF and for Re = 0.01. The phase space attractors undergo a reflection upon changing the direction of the initial motion of the particle.

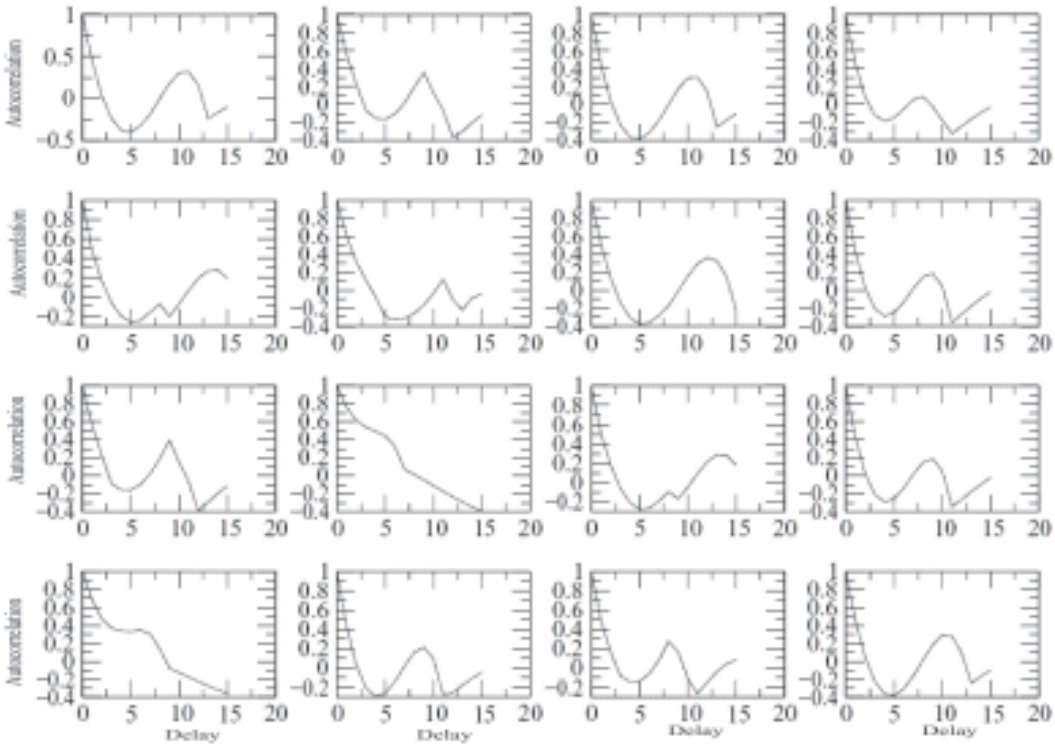

Figure 3.6 The Autocorrelation function plots for Re = 0.01.The time delay is obtained at the first zero of the autocorrelation function, or as the value of the delay where autocorrelation reduces to 1/e of its initial value.

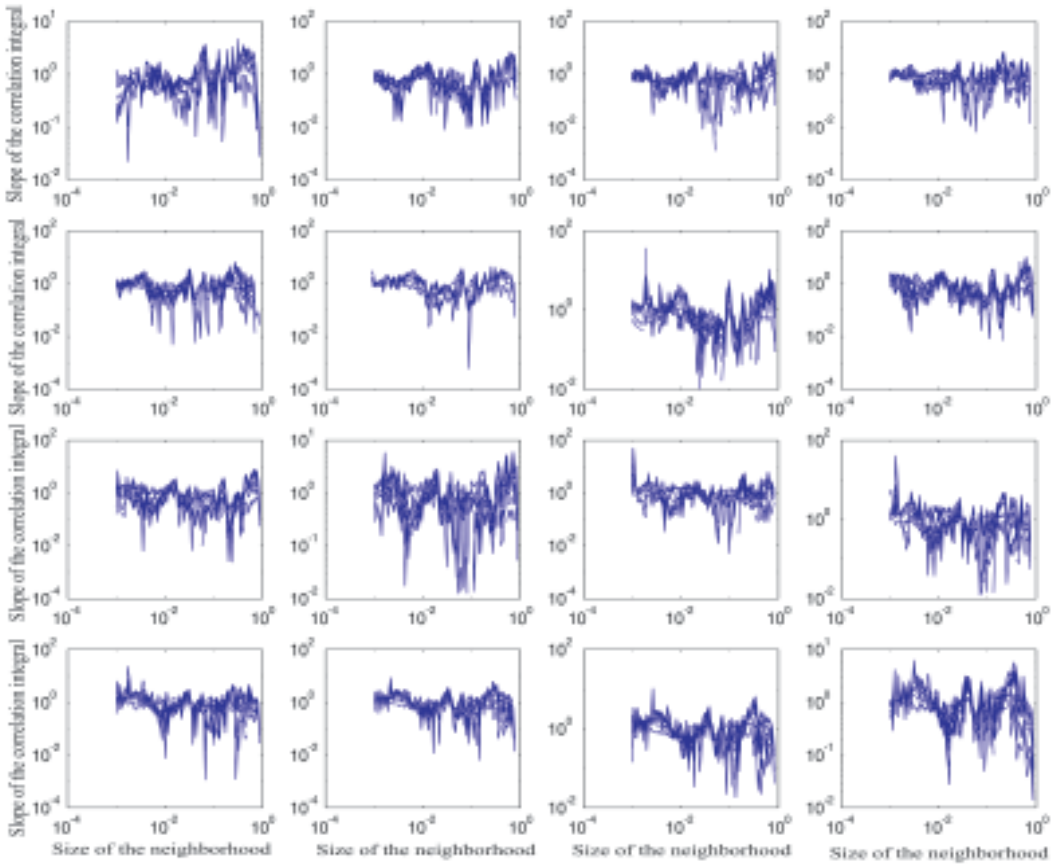

Figure 3.7 The Correlation Dimension plot for Re = 0.01. The embedding dimension is obtained by Taken's theorem that it is atmost (2d+1), where d is the correlation dimension. There exists a range of values of the neighborhood where the slope of the correlation integral is approximately constant. The nearly constant slope of the correlation integral is an estimate of the correlation dimension.

Table 3.1 This table shows the time delay, embedding dimension and the nearest integer to the correlation dimensions obtained for Re = 0.01 and for various Re_F ranging from 0.01 to 0.6. Such a table is obtained for the values of Re ranging from 0.01 to 0.6, here we present just an example of Re = 0.01.

Re	Re_F	One step prediction error		False nearest neighbors	d2-plot	Autocorrelation function	Average mutual information
		Delay	Embedding dimension	Embedding dimension	Correlation dimension	Delay	Delay
0.01	0.01	5	6	6	2	8	2
0.01	0.02	7	4	8	2	3	4
0.01	0.03	6	5	8	2	3	3
0.01	0.04	9	10	7	2	3	4
0.01	0.05	1	2	7	2	3	3
0.01	0.1	3	6	7	2	8	3
0.01	0.15	2	5	8	2	4	3
0.01	0.2	5	6	8	4	3	3
0.01	0.25	6	5	8	4	3	3
0.01	0.3	6	4	7	3	3	3
0.01	0.35	9	3	7	4	3	4
0.01	0.4	7	7	8	3	3	4
0.01	0.45	6	3	9	3	3	3
0.01	0.5	9	7	8	3	3	3
0.01	0.55	5	10	8	4	2	3
0.01	0.6	6	3	8	3	3	3

results had shown the existence of a preferred direction in the problem. This direction did not depend on any physical aspect of the problem. In our new simulations we noted that when we reversed the direction of the initial motion, we obtained a reflection of the attractor relative to the velocity axis. This shows that there is a direction in the problem and that it depends on the direction of the initial motion. We present here an example of the attractors obtained for Re = 0.01 and for various Re_F ranging from 0.01 to 0.6 in Figure 3.5. Figure 3.5 also shows the effect of reversing the initial directions of the force on the spherical particle. That is, the figure shows the attractors for the two different initial directions of the external force. Figure 3.5. shows the reflection of the two attractors when the initial direction of the forces are in opposite direction.

There is negligible drift in the motion of the spherical particle. At low Reynolds numbers, the spherical particle oscillates around a mean position due to periodic forcing, and this is shown in the phase plots of Figure 3.5.

We performed several tests on the time series of displacement versus time, which was obtained from the simulations. We have attempted to test for deterministic chaos in the time series. Using TISEAN, a Nonlinear Time Series Analysis software by Hegger et. al, we obtained the time delay and embedding dimensions. The time delay was estimated by the Autocorrelation and the Average Mutual Information. The embedding dimension was estimated using False Nearest Neighbors and Correlation Dimension methods. Figure 3.6 gives the autocorrelation plots for Re = 0.01. Figure 3.7 shows the Correlation Dimension (d2) plot for Re = 0.01. The time delay and embedding dimension were also obtained by the evaluation of minimum error in one Step ahead prediction. Table 3.1

shows the various estimates obtained of the time delay and the embedding dimensions for Re = 0.01. We have performed these analyses on all the attractors and time series obtained for Re ranging from 0.01 to 0.6. Finally all these computations lead to the computation of a Lyapunov exponent which is slightly greater than zero, which shows the possibility of existence of deterministic chaos in the system.

We are currently in the process of trying to determine the route to chaos, if it exists in our problem.

T R Ramamohan, I S Shivakumara
K Madhukar

3.3 Finite Element Modeling of Thermomechanical Behavior and Microstructural Evolution in Steel

There is a strong requirement for a comprehensive modelling approach in which finite element analysis (FEA) of plastic deformation and temperature during thermomechanical processes of metals must be closely coupled with microstructure evolution model to allow prediction of evolving microstructure and final mechanical properties. Some recent efforts have been made by researchers towards this objective but lot of further work is still necessary in this subject. Further, the details of model and computation in these studies are not available in open literature.

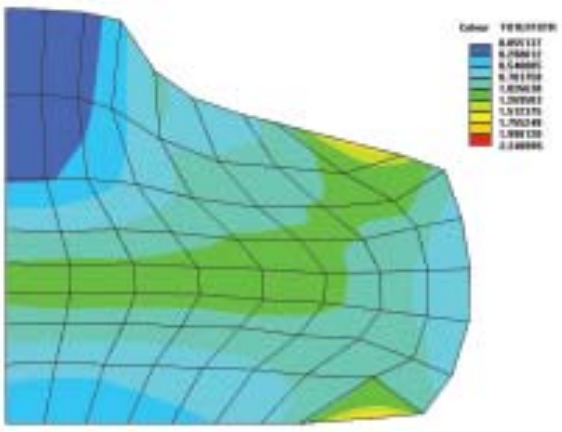

Figure 3.8 Effective strain in a cylindrical steel billet after die displacement of $0.6H_o$ during spike forging of the billet in an impression die containing a central cavity.

The overall objective of the proposed project study is to perform a comprehensive study of thermomechanical behavior (plastic deformation and thermal analysis) of steel during hot forming process using the finite element method and integrate the thermomechanical process model with a microstructure evolution model to predict the microstructure and final mechanical properties.

Figure 3.9 Effective strain in a steel strip after the strip has traveled into the roll gap a distance of approximately 50% of contact length between roll and strip.

A Finite element formulation for rigid plastic and rigid-viscoplastic metal forming problems is developed. An Arbitrary Lagrangian Euler formulation is used to model large deformations and mechanical contacts. Four-node, eight noded and nine-noded quadrilateral elements (both 2D and axisymmetric) were formulated for the study. The flow behavior of the metal is modeled as a function of strain rate, strain and temperature.

The above formulation was implemented in a versatile and user-friendly FEM computer code "*FACS*" (having over one lakh statements) developed by the author in visual C++ programming language during and after his Ph.D. program. Both direct iteration method and incremental-iterative Newton-Raphson method were implemented for solving non-linear equations. An appropriate remeshing technique has been implemented to overcome severe distortions in finite elements during simulation steps. The code is also augmented with graphics facilities for solid-model plotting, mesh plotting and results plotting (contour as well as vector plots) during each simulation

step. The software has been validated by comparing the results with those available in literature for an example problem of upsetting between flat dies.

Some example problems of axisymmetric forging (i.e. simple upsetting of circular cylinder between flat dies, upsetting with shaped (inclined) dies and spike forging of cylindrical billet in an impression die containing a central cavity) and plane strain rolling of S45C stainless steel are solved. Metal flow, effective strain rate and effective strain distributions inside the workpiece are calculated at each simulation step. A few simulations results are presented in Figures (3.8) and (3.9).

Surendra Kumar

3.4 Analysis of Impact response and Damage in Laminated Composite Shell by Finite Element Method

Resistance of the damage caused by low and moderate velocity non-penetrating impact is an important consideration in the design of fibre-reinforced plastic laminated composite structure. This type of damage in the form of matrix cracking and delamination is often internal and not visible but causes substantial drops in the strength and stability of the structure.

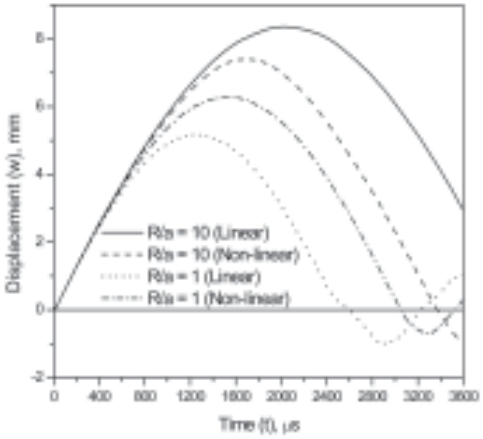

Figure 3.10 Centre displacement in graphite/epoxy cylindrical shells ($[90_4/0_8/90_4]$) (a = b = 300 mm; R = 10a and R = a), with clamped edges and impacted by blunt-ended steel cylinder of nose radius 5 mm and mass 300 gm having initial velocity of 7 ms^{-1}.

Although extensive literature are available on impact response of laminated plates and shells, those dealing with impact damage on shells and curved laminated panels are relatively sparse and in particular, relatively few investigators have studied geometrical non-linear effects on curved laminated structures.

In this investigation, a non-linear finite element analysis is carried out to predict impact response and impact-induced damage in curved composite laminate subjected to transverse impact by a metallic impactor. An eight-noded isoparametric quadrilateral shell element incorporating geometrical non-linearity due to large deflection is implemented based on total Langragian approach. The non-linear system of equations resulting from large displacement formulation and non-linear contact law are simultaneously solved using Newton-Raphson incremental-iterative method. Example problems of graphite/epoxy cylindrically curved shell are considered with parametric variations and influence of geometrical non-linearity on the impact response and resulting damage is demonstrated.

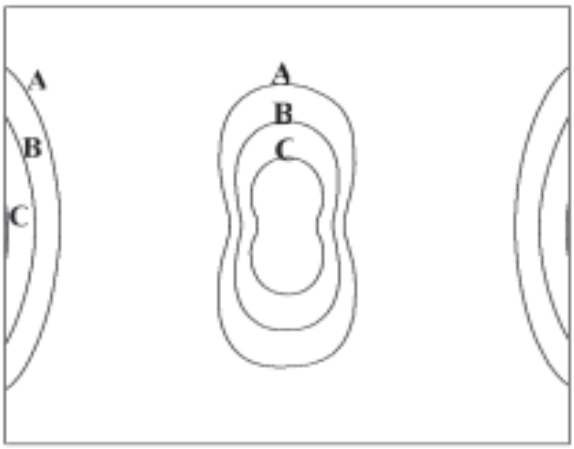

Figure 3.11 Maximum strength ratio, e_m in bottom $[90_4]$ ply of $[90_4/0_8/90_4]$ cylindrical shells (dimensions: a = b = 100 mm) having curvature R/a = 1, with clamped edges and impacted by 200 gm mass at a velocity of 5 ms^{-1}. (e_m values: A = 0.2, B = 0.5, C = 1.0).

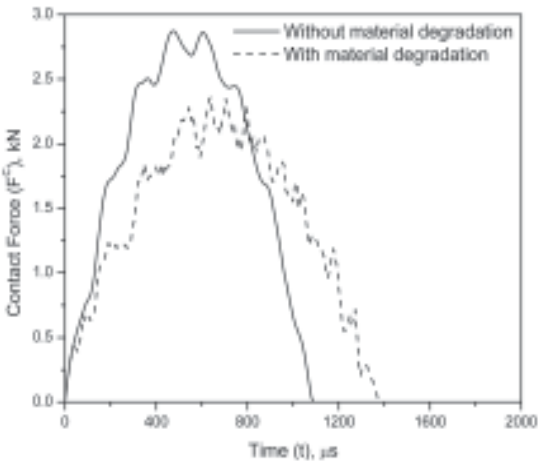

Figure 3.12 Effect of material degradation on contact force in graphite/epoxy cylindrical shell ([$90_4/0_8/90_4$] lay-up) ($a = b = 100$ mm; $R = a$; non-linear analysis), with clamped edges and impacted by blunt-ended steel cylinder of nose radius 5 mm and mass 200 gm having initial velocity of 5 ms^{-1}.

The study also includes incorporation of appropriate stiffness reduction of the damaged region in the laminate as the solution progresses with time.

Few important results are depicted in Figures (3.10) to (3.12) with self-explanatory legends.

Surendra Kumar

3.5 Finite Element Modelling for Dynamic Analysis of an Aircraft Fuselage Structure

Improved mid-frequency structural vibration and acoustic response predictions are required for design optimization and noise control applications in the aerospace. Advances in computer technology provide the capability to solve FE analyses of increasing complexity. The ability to extend the valid frequency range for FE based structural dynamic predictions using detailed models of the components and attachment interfaces has been examined. Normal mode predictions for different finite element representations of components and assemblies are compared with experimental results to assess the most accurate techniques for modeling aircraft fuselage type structures. The aim of the work is to Model the parts of the fuselage structure and the fuselage and obtain the normal mode predictions for finite element representations of components and assembly are compare with experimental results to assess the most accurate techniques for modeling aircraft fuselage structures. Our interest has been focused on stiffened aircraft fuselage structures(Figure 3.13). The structure is the Aluminum Testbed

Table 3.2 Experimental and numerical natural frequencies for the Fuselage Structure

Mode	Finite element ObtainedFrequency, Hz	Modal test Result frequency, Hz
7	54.648	50.82
8	54.648	51.176
9	57.688	53.462
10	57.688	54.287
11	110.73	100.146
12	110.73	102.123
13	148.59	141.375
14	148.59	142.348
15	161.92	152.39
16	161.92	152.411
17	172.43	160.102
18	172.43	161.829
19	198.93	183.553
20	198.93	204.342

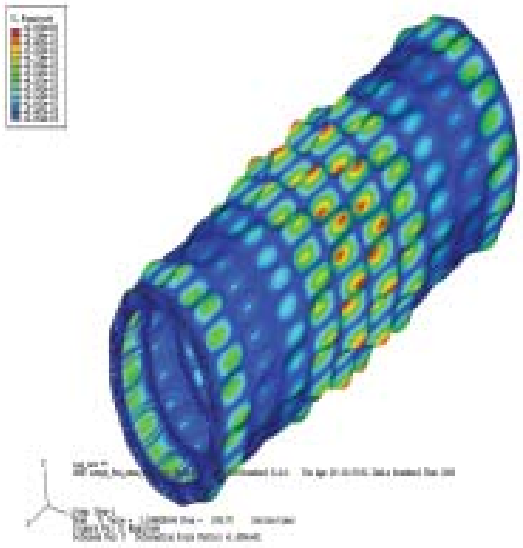

Figure 3.13 Fuselage Predicted mode shape at 286.70 Hz

Cylinder (ATC). The cylindrical section of the ATC is an all-aluminum structure that is 12 feet in length and 4 feet in diameter. The shell consists of a 0.040-inch thick skin that is stiffened by 11 ring frames and 24 equally spaced longitudinal stringers. Double lines of rivets and epoxy are used to attach the skin to the frames and stringers. The bay responses are the focus of the fuselage panel correlation efforts. Comparisons for the numerical and experimental natural frequencies for the ATC baseline cylinder are provided for the first fifteen modes in Table 3.2. The local bay modes of the Fuselage structure are Shown Below. The table shows that they are in excellent agreement with the experimental results.

P Rajesh, V Senthilkumar, G Prathap and H V Lakshiminarayana

3.6 Vibration Analysis of Folded Plates

Folded plates or plate assemblies have wide practical applications in aerospace, marine and civil engineering due to substantial increase in the stiffness, buckling and vibration capacities of the folded plates (Figure 3.14) over their flat form counterparts. A nine nodded plate element with five degrees of freedom per node is appended to an additional drilling degree of freedom has been developed to study the free vibration characteristics of folded plates. A 6 X 6 transformation matrix has been derived to transform the element stiffness and element mass matrix before assembling the whole system matrix. The element is based on first order shear deformation theory with transverse shear correction factor of 5/6. The frequencies have been compared with available literature and the new results are proposed to be used for future validation purpose.

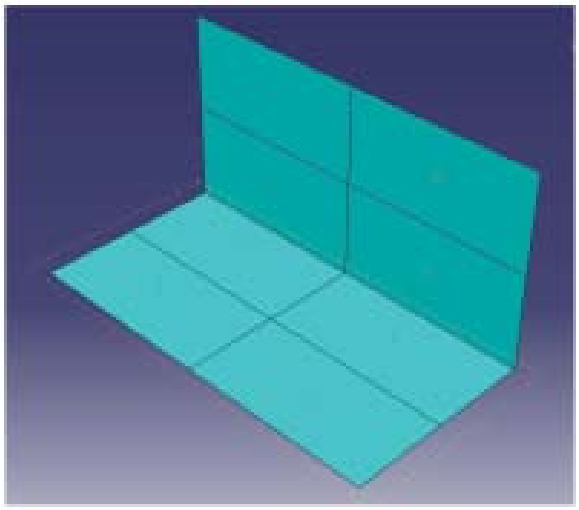

Figure 3.14 Folded plate geometry

The free vibration frequencies of isotropic single-fold are presented in table 3.3. The length of the cantilever folded plate is 1.5m and E=10.92e+9 N/m^2, v=0.3 and mass density is 1000kg/m^3.

Table 3.3 Non dimensional frequencies

PlateDescription	ModeNumber	Mesh size	Present QUAD9	Ritz Method	FE Transfer Matrix Method
Flat Plate	1	4x4	0.0200	0.0200	0.0201
	2		0.0489	0.0492	0.0493
	3		0.1230	0.1235	0.1234
	4		0.1567	0.1566	0.1577
	5		0.1784	0.1787	0.1796
One folded plate 90	1	4x2	0.0491	0.0491	0.0492
	2		0.0972	0.0971	0.0977
	3		0.1888	0.1786	0.1794
	4		0.2188	0.2084	0.2101
	5		0.3584	0.3558	0.3573

V Senthilkumar, S C Pradhan and G Prathap